Available online at www.sciencedirect.com
ScienceDirect
Journal of Sound and Vibration 307 (2007) 202–225
JOURNAL OF SOUND AND VIBRATION
www.elsevier.com/locate/jsvi

Source identification system based on the time-domain nearfield equivalence source imaging: Fundamental theory and implementation

Mingsian R. Bai*, Jia-Hong Lin

Department of Mechanical Engineering, National Chiao-Tung University, 1001 Ta-Hsueh Road, Hsin-Chu 300, Taiwan

Received 5 September 2006; received in revised form 10 April 2007; accepted 30 June 2007

Abstract

A nearfield equivalence source imaging (NESI) technique is proposed to identify locations and strengths of noise sources. The NESI is based on the time-domain formulation that applies not only to stationary but also a transient noise. Multichannel inverse filters are designed using the least-square optimization. Tikhonov regularization is called for to mitigate the ill-posedness inherent in the underdetermined model-matching problem. The design parameters such as array aperture, microphone spacing, focal point spacing and distance of projection have profound impact on the resulting sound image resolution. The distance of reconstruction (DOR) is selected according to the condition number of the propagation matrix. A windowing design is also suggested to cope with boundary defocusing problem. Beam pattern is calculated for the inverse filters with window design. In addition, a modified approach based on focal point points is devised to avoid the singularity problem in reconstructing sound images. The multichannel inverse filters are implemented in light of a highly efficient state-space minimal realization technique. The NESI is applicable to one-dimensional (1D) linear array, two-dimensional (2D) rectangular array and even other arrays of irregular geometries. As indicated by the simulation results, the proposed NESI technique proves effective in the identification of noise sources.

1. Introduction

Noise source identification (NSI) is a vital step prior to a successful noise control program. Noise sources largely fall into two categories: vibration-induced noise and flow-induced noise. Examples of the first category include noise from rotating machinery, impact noise, noise due to structural resonance, braking squeal, etc., while examples of the second category include fan noise, pump noise, jet noise, etc. NSI techniques have been studied extensively by acoustical engineers. Among the NSI methods, sound field visualization techniques are particularly useful in estimating the source position and the source strength. In addition to NSI, sound field visualization techniques also find applications in non-destructive evaluation [1,2], underwater imaging [3,4], and machine diagnosis [5,6] and so forth.

*Corresponding author. Fax: +886 3 5720634.
E-mail address: msbai@mail.nctu.edu.tw (M.R. Bai).

0022-460X/$ - see front matter © 2007 Elsevier Ltd. All rights reserved.
doi:10.1016/j.jsv.2007.06.025

Nearfield acoustical holography (NAH), a celebrated technique for NSI was pioneered by Maynard and Williams in early 1980s [7,8]. The technique enables reconstructing the three-dimensional (3D) sound field from the two-dimensional (2D) hologram data scanned above the source surface. In comparison with another commonly used NSI technique, the sound intensity method [9], the NAH provides a more global view of noise distribution and the relative strength. The NAH has now been commercialized by Brüel and Kjael with a new name, spatial transformation of sound field (STSF) [10–12]. A comprehensive treatment of NAH can be found in the monograph by Williams [13]. While the NAH represented an elegant solution in the sound field visualization techniques, there are a number of limitations in the original version of the NAH. Most of these limitations stem from the fact that the NAH transformation relies on the two-dimensional fast Fourier transform (2D FFT) between the physical space and the wave number space. This implies that stationary frequency-domain pressure phasors must be available and the scanned grid points must be equally spaced on a planar rectangular area [14]. Numerical artifacts such as aliasing problem arising in FFT may adversely affect the accuracy of imaging. This situation is further aggravated in practical application, where the number of sensor and data acquisition channel is usually quite limited due to cost consideration. To deal with these limitations, the NAH was later extended to problems with irregular geometries [15,16] and non-stationary noise [12]. The inverse reconstruction techniques have been extended to deal with irregular shaped sources by applying singular value decomposition (SVD) to the inverse boundary element method (IBEM) [17]. In spite of all that, one to three times of FFT has to be carried out with the microphone spacing kept less than half of a wavelength to avoid the spatial aliasing problem. This requires large number of microphones and enormous processing power to cover a reasonable source area. In addition, latency becomes more of a problem when one has to measure a transient noise such as pass-by noise in real time.

In this paper, a new technique based on a multichannel inverse filtering idea is proposed to address the aforementioned limitations of the NAH. This technique termed the nearfield equivalence source imaging (NESI) is essentially a unified approach of the NAH and a beamformer. The NESI differs from the previous approaches in that, without resorting to Fourier transformation, it seeks to reconstruct the sound field directly by forming a focused beam in the nearfield using time-domain filtering. The major benefit resulting from this fundamental difference is that many of the limitations associated with FFT are eliminated in the new method. It should be pointed out here this paper is not the first application of acoustical beamformer to the NSI problems. An early acoustical beamformer developed by the author was based on the delay and sum algorithm, the minimum variance distortionless response (MVDR) algorithm, and the multiple signal classification (MUSIC) [18]. The beamforming in the conventional sense is generally based on the assumption that the incoming waves are plane waves from the farfield. A basic beamforming approach is thus to 'delay' (according to the difference of propagation distance between sensors) and 'sum' the signals picked up at each sensor. As a result, array output with enhanced signal-to-noise ratio is obtained by this 'time-alignment' process. Maximum array output indicates the potential source directions. By this nature, the conventional beamforming approach is well suited to localizing large-scale sources situated in the farfield, instead of sources in the nearfield. Commercial beamformers also emerge in the market for the NSI purpose [19,20]. However, these beamformers are mostly FFT-based and suited for farfield imaging with coarse spatial resolution. The NESI proposed in the paper combines the merits of the NAH and conventional beamformers. Not only sound field processing is entirely carried out in the time-domain but also nearfield details can be reconstructed. This technique is applicable to noise sources of all kinds, including narrowband, broadband, stationary, and transient types.

The heart of the NESI is the design of multichannel inverse filters based on an equivalent source concept [21,22]. The design procedure employed in the paper is along the same line as that used in designing the so-called cross-talk cancellation system (CCS) [23] in spatial audio processing. Least-square optimization in association with Tikhonov regularization is exploited to overcome the ill-posedness inherent in the generally underdetermined problem. Windowing is also used in the design phase to mitigate the boundary defocusing problem. The singularity on reconstructing the sound field on the source surface is circumvented by using a retreated focal point technique. The sound pressure, the particle velocity, and the sound intensity can be calculated on the reconstructed surface by NESI in conjunction with the retreated focal point method.

Although the digital signal processing (DSP) technology has advanced to a level that permitted the implementation of the NESI. Substantial simplification is possible by exploiting an eigensystem realization

algorithm (ERA) to accelerate the multichannel filtering of the NESI. Numerical simulations were undertaken to examine the NESI for the 1D and 2D array configurations. The results and design guidelines will be summarized in the conclusions.

2. Theory and methods

2.1. Inverse filtering from a multi-channel model-matching perspective

The pressure of a linear sound field can be represented by a simple layer potential [13] as

$$p(\mathbf{x}) = \int_S \sigma(\mathbf{y}) G(\mathbf{x},\mathbf{y})\,\mathrm{d}S(\mathbf{y}), \tag{1}$$

where

$$G(\mathbf{x},\mathbf{y}) = \frac{\mathrm{e}^{-\mathrm{j}kr}}{r} \tag{2}$$

being the free-space Green's function between the source point $\mathbf{y}$ and the field point $\mathbf{x}$, $r = |\mathbf{x}-\mathbf{y}|$, $k = 2\pi f/c$ is the wave number, c is the speed of the sound and f is the frequency, $\sigma(\mathbf{y})$ is an unknown source strength of the point source distribution, and S is the source surface. Straightforward discretization of Eq. (1) leads to

$$\begin{aligned} p(\mathbf{x}) &= \int_S \sigma(\mathbf{y}) G(\mathbf{x},\mathbf{y})\,\mathrm{d}S(\mathbf{y}) \approx \sum_{i=1}^{I} \int_{S_i} \sigma(\mathbf{y}) G(\mathbf{x},\mathbf{y})\,\mathrm{d}S(\mathbf{y}) \\ &\approx \sum_{i=1}^{I} [\sigma(\mathbf{y}_i)\hat{S}_i] G(\mathbf{x},\mathbf{y}_i) = \sum_{i=1}^{I} q_i G(\mathbf{x},\mathbf{y}_i), \end{aligned} \tag{3}$$

where $\hat{S}_i$ is the area of the ith element, $\mathbf{y}_i \in \hat{S}_i$, $q_i = \sigma(\mathbf{y}_i)\hat{S}_i$ represents the strength of the ith point source, and I is the number of focal point. It should be borne in mind that these virtual point sources only constitute an equivalent discrete representation in that they would produce the same field, $p(\mathbf{x})$. The amplitudes of these point sources represent relative source strength associated with each source location, which could be due in part to physical sources and/or the effects nearby boundary reflection. These I virtual sources are assumed to be located at the desired focal points.

Consider a NSI problem depicted in Fig. 1(a) and (b), where sound pressures radiated by a source are received at the M microphones. The measured sound pressures and the source strengths are related by

$$\begin{bmatrix} p(\mathbf{x}_1) \\ p(\mathbf{x}_2) \\ \vdots \\ p(\mathbf{x}_M) \end{bmatrix} = \begin{bmatrix} G(\mathbf{x}_1,\mathbf{y}_1) & G(\mathbf{x}_1,\mathbf{y}_2) & \cdots & G(\mathbf{x}_1,\mathbf{y}_I) \\ G(\mathbf{x}_2,\mathbf{y}_1) & G(\mathbf{x}_2,\mathbf{y}_2) & \cdots & G(\mathbf{x}_2,\mathbf{y}_I) \\ \vdots & \vdots & \ddots & \vdots \\ G(\mathbf{x}_M,\mathbf{y}_1) & G(\mathbf{x}_M,\mathbf{y}_2) & \cdots & G(\mathbf{x}_M,\mathbf{y}_I) \end{bmatrix} \begin{bmatrix} q_1 \\ q_2 \\ \vdots \\ q_I \end{bmatrix} \tag{4}$$

or, in matrix form

$$\mathbf{p} = \mathbf{G}\mathbf{q}. \tag{5}$$

Since the number of microphones is usually no greater than that of the focused points ($M \leqslant I$), the propagation matrix $\mathbf{G} \in C^{M\times I}$ could be non-square and the problem could be underdetermined. The purpose here is to estimate $\mathbf{q}$ based on the measurement $\mathbf{p}$. This can be regarded as a model matching problem depicted in Fig. 1(c), where the propagation matrix $\mathbf{G}$ has the source strength $\mathbf{q} \in C^{I\times 1}$ and the pressure measurement $\mathbf{p} \in C^{M\times 1}$ as its input and output, $\mathbf{e} \in C^{J\times 1}$ is the matching error where the J is number of focal points, $\mathbf{C} \in C^{J\times M}$ is the inverse filter matrix, and $\mathbf{W} \in C^{J\times I}$ is the matching model. With the most basic choice of $\mathbf{W}$ being the identity matrix $\mathbf{I}$, the problem reduces to, given $\mathbf{p}$ and $\mathbf{G}$, finding an inverse filter $\mathbf{C}$ such that $\mathbf{CG} \approx \mathbf{W} = \mathbf{I}$ and hence

$$\hat{\mathbf{q}} = \mathbf{C}\mathbf{p} = \mathbf{C}\mathbf{G}\mathbf{q} \approx \mathbf{q}. \tag{6}$$

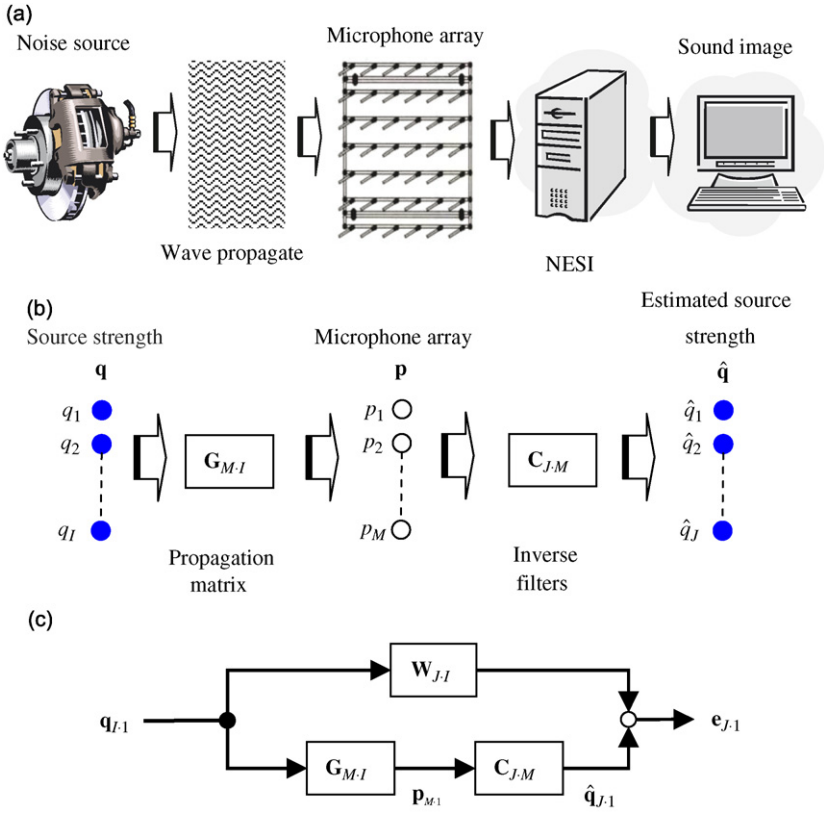

Fig. 1. The nearfield equivalence source imaging (NESI): (a) illustration for noise source identification problem using the NESI, (b) the block diagram of inverse filtering process, and (c) the inverse filtering process viewed as a model matching problem.

2.1.1. Least-square optimization

Similar to the deconvolution process in NAH, the system matrix **G** is usually ill-conditioned and even non-square. This calls for the need of optimization with proper regularization. The problem considered herein can be put into the following optimization formalism:

$$\min_{\mathbf{C}} \|\mathbf{W}-\mathbf{C}\mathbf{G}\|_F^2, \tag{7}$$

where $\|\cdot\|_F^2$ symbolizes the Frobenius norm [24] defined as, for an $J\times I$ matrix **A**,

$$\|\mathbf{A}\|_F^2=\sum_{i=1}^{I}\sum_{j=1}^{J}|a_{ji}|^2=\sum_{i=1}^{I}\|\mathbf{a}_i\|_2^2. \tag{8}$$

Hence, the minimization problem of Frobenius-norm can be converted to the minimization problem of the 2-norm by partitioning the matrices into columns. Since there is no coupling between the columns of matrix **C**, the minimization of the square of the Frobenius-norm of the entire matrix **G** is tantamount to minimizing each column independently:

$$\min_{\mathbf{C}} \|\mathbf{W}-\mathbf{C}\mathbf{G}\|_F^2=\min_{\mathbf{c}_i}\sum_{i=1}^{I}\left\|\mathbf{w}_i^H-\mathbf{G}^H\mathbf{c}_i^H\right\|_2^2,\quad i=1,2,\ldots,I, \tag{9}$$

where $\mathbf{w}_i$ and $\mathbf{c}_i$ denote the ith columns of the matrices **W** and **C**, respectively, the superscript "H" denotes the Hermitian transpose. The least-squares solution to the problem above are given as

$$\mathbf{c}_i^H=(\mathbf{G}^H)^{+}\mathbf{w}_i^H,\quad i=1,2,\ldots,I, \tag{10}$$

where the superscript "+" denotes the pseudo-inverse [19]. This optimal solution in least-square sense can be assembled into a more compact matrix form:

$$[\mathbf{c}_1 \quad \mathbf{c}_2 \quad \cdots \quad \mathbf{c}_I]^H = (\mathbf{G}^H)^+ [\mathbf{w}_1 \quad \mathbf{w}_2 \quad \cdots \quad \mathbf{w}_I]^H \tag{11}$$

or

$$\mathbf{C} = \mathbf{W}\mathbf{G}^+ \tag{12}$$

If the system matrix $\mathbf{G}$ is of full-row rank, the pseudo-inverse is given as

$$\mathbf{G}^+ = \mathbf{G}^H(\mathbf{G}\mathbf{G}^H)^{-1}. \tag{13}$$

Note that $\mathbf{G}^+$ is also the right inverse in that $\mathbf{G}\mathbf{G}^+ = \mathbf{I}$. Nevertheless, if $\mathbf{G}$ is not of full-row rank, Tikhonov regularization [25,26] can be used to avoid singularity of $\mathbf{G}\mathbf{G}^H$. Specifically,

$$\mathbf{C} = \mathbf{W}\mathbf{G}^H(\mathbf{G}\mathbf{G}^H + \beta\mathbf{I})^{-1}, \tag{14}$$

where $\beta \geqslant 0$ is a regularization parameter that can either be a constant or frequency-dependent [23]. Not only making the optimal filters easier to calculate numerically, such regularization approach can also shorten the FIR filters.

In this paper, the right inverse is used for the under-determined problem ($M \leqslant I$), which is different from the setting in Ref. [27], where an over-determined problem ($I \leqslant M$) is assumed. If, instead, left inverse is used in the present formulation, the matrix product $\mathbf{G}^H\mathbf{G}$ can become extremely rank-deficient. Heavy regularization would be required to maintain numerical stability.

One problem encountered with the simple choice of the matching model $\mathbf{W} = \mathbf{I}$ is that defocusing problem may arise. This is a frequently encountered problem particularly in the neighborhood of the boundary of the focal surface. To resolve the problem, a modified matching model is suggested as follows. In addition to the focal points, the outer ring of the focal surface is padded with "null points" to restrain the level of reconstructed data outside the boundary, as shown in Fig. 2. This is analogous to the windowing technique in digital filter design. Thus, the matching model is modified into

$$\mathbf{W} = \left[\begin{array}{ccc} 1 & \cdots & 0 \\ \vdots & \ddots & \vdots \\ 0 & \cdots & 1 \\ \hline 0 & \cdots & 0 \\ \vdots & \ddots & \vdots \\ 0 & \cdots & 0 \end{array}\right]_{J \times I}, \tag{15}$$

where I diagonal entries "1" correspond to the focal points and "0" entries at the bottom half correspond to the null points. With this choice of $\mathbf{W}$, it can be shown that

$$\hat{\mathbf{q}} = \mathbf{W}\mathbf{q} = [q_1 \quad q_2 \quad \cdots \quad q_I \quad 0 \quad \cdots \quad 0]^{\mathrm{T}}. \tag{16}$$

It is noted that the inverse filters $\mathbf{C}$ obtained in Eq. (14) are still in the frequency-domain. Inverse FFT is called for to convert and truncate these frequency response functions into finite impulse response (FIR) filters in the time-domain. In this step, circular shift is needed to ensure that the resulting filters are causal filters. Now that the inverse filters are available, the strength of the virtual sources at the focal points can be calculated by using multichannel convolution:

$$\hat{q}_i(n) = \sum_{m=1}^{M} p_m(n) \circledast C_{im}(n), \quad 1 \leqslant i \leqslant I, \tag{17}$$

where n denotes the discrete-time index, $C_{im}(n)$ denotes the impulse response of the imth inverse filter and "$\circledast$" denotes the convolution operator. The thus obtained virtual source strength at the focal point will serve as the basis for subsequent sound field reconstruction.

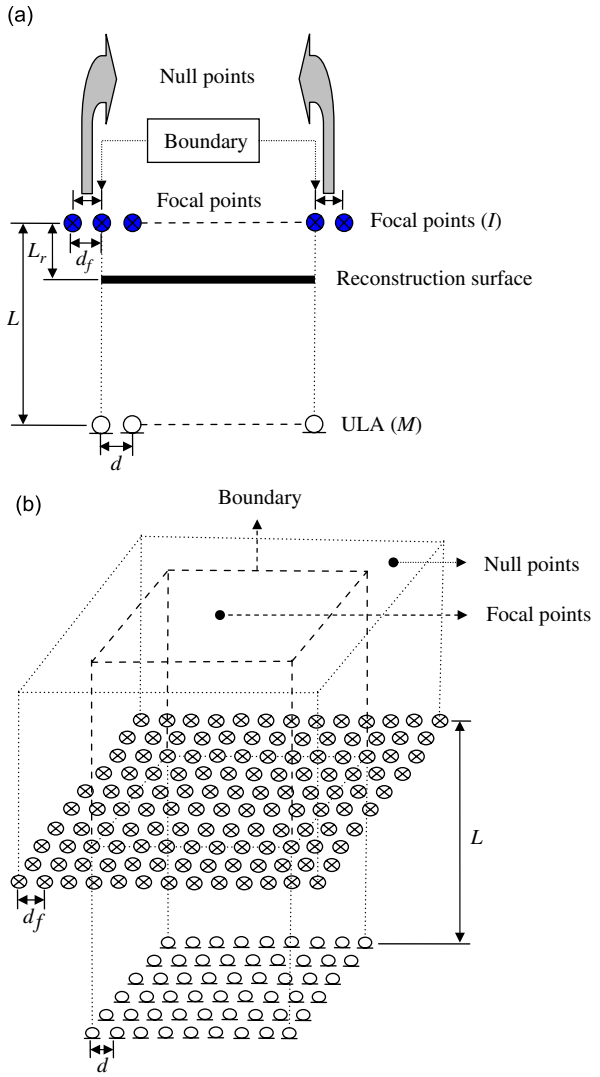

Fig. 2. The array structure: (a) 1D ULA and (b) 2D URA.

2.1.2. Beam pattern

In the NESI design, it is revealing to calculate the beam pattern of array, which shows the idea of spatial resolution of the beamformer. The beam pattern can be obtained by scanning on the focal surface by using a point source of the form of Eq. (2). First, the inverse filter matrix is calculated in accordance with decided array parameters by Eq. (14). Second, let $\mathbf{p}$ be the sound pressure produced by the moving point source and received at the microphones. Finally, the beam pattern of each focal point corresponds to the respective element of the vector $\mathbf{b} = \mathbf{C}\mathbf{p}$. The number of beam patterns is equal to the number of focal points.

2.1.3. Retreated focal points

A subtle but vital aspect of the NESI outlined above is the positioning of the focal surface. An intuitive approach is simply to choose the surface of the physical source as the focal surface. However, this would present a problem because the point source model in Eq. (2) becomes singular when it comes to the computation of acoustical variables such as pressure, particle velocity, and intensity. To overcome this problem, we choose a focal surface slightly behind, e.g., $L_r = d/20$, where d is spacing of microphones, the

physical source surface, as shown in Fig. 2(a). With these "retreated" focal points, the distance between the source points and the field points could never be zero. According to the Huygen's principle [28], the virtual source idea is merely a representation of sound field, which does not have to coincide with the physical surface, and the resulting sound field is equivalent. It follows that the sound pressure on the reconstruction surface can be calculated in the time-domain using

$$p(\mathbf{x},n)=\sum_{i=1}^{I}\frac{\hat{q}_i(n-\Delta_i)}{r_i}, \tag{18}$$

where $\mathbf{x}$ is the position vector of the Field point on the reconstruction surface, r_i is the distance between the ith virtual source and the Field point $\mathbf{x}$, and $\Delta_i=\mathrm{int}(r_i/c)$ is the time delay rounded to the nearest integer. As will be shown later, this retreated focal point approach facilitates reconstructing the sound image with fine spatial resolution.

2.1.4. Acoustical variables

In addition to sound pressure, particle velocity, and sound intensity can be calculated by using the NESI technique. The last two acoustical variables are deemed more effective in the context of the NSI application. For simplicity, consider only one virtual point source on the focal point surface. Let $\mathbf{x}_0$ and $\mathbf{x}$ be the position vectors of the virtual source and the field point on the reconstruction surface, respectively. The sound pressure at the field point produced by the point source of strength $\hat{q}(\omega)$ can be written as the following frequency-domain expression:

$$p(\mathbf{x},\omega)=\hat{q}(\omega)\frac{\mathrm{e}^{-\mathrm{j}kr}}{r}, \tag{19}$$

where $k=\omega/c$ is wave number, and $r=|\mathbf{x}-\mathbf{x}_0|$. Form the Euler equation [28], the particle velocity at the normal direction to the reconstruction surface follows:

$$\begin{aligned}u_n(\mathbf{x},\omega)&=\frac{-1}{\mathrm{j}\rho\omega}\frac{\partial}{\partial n}p(\mathbf{x},\omega)\\&=\frac{-1}{\mathrm{j}\rho\omega}\mathbf{n}\cdot\nabla_{\mathbf{x}}\left(\frac{\hat{q}(\omega)\mathrm{e}^{-\mathrm{j}kr}}{r}\right)\\&=\frac{1}{\mathrm{j}\rho\omega}(\mathbf{n}\cdot\mathbf{e}_r)\left(\mathrm{j}k+\frac{1}{r}\right)p(\mathbf{x},\omega),\end{aligned} \tag{20}$$

where ρ is the density of air and $\mathbf{e}_r=(\mathbf{x}-\mathbf{x}_0)/r$. Rewrite this equation in the Laplace domain

$$u_n(\mathbf{x},t)=\frac{1}{\rho c}(\mathbf{n}\cdot\mathbf{e}_r)\frac{s+(1/\tau)}{s}p(\mathbf{x},t), \tag{21}$$

where $\tau=r/c$ being the time delay. Here the DC pole($s=0$) behaves like an integrator, which could cause problems. To fix this, a highpass filter is introduced by modifying Eq. (21) into

$$\begin{aligned}u_n(\mathbf{x},t)&=\frac{1}{\rho c}(\mathbf{n}\cdot\mathbf{e}_r)\frac{s+(1/\tau)}{s}\frac{s}{s+(1/\tau_0)}p(\mathbf{x},t),\quad \tau_0\gg 0\\&=\frac{1}{\rho c}(\mathbf{n}\cdot\mathbf{e}_r)F(s)p(\mathbf{x},t),\end{aligned} \tag{22}$$

where

$$F(s)=\frac{s+(1/\tau)}{s+(1/\tau_0)},\quad \tau_0\gg 0. \tag{23}$$

It follows that the normal velocity u_n can be obtained by properly filtering the sound pressure with $F(s)$. To facilitate digital implementation, a discrete-time filter can be obtained by the Prewarped Bilinear Transform [29]:

$$F(z)=F(s)\big|_{s=g\frac{z-1}{z+1}}=\frac{\tau_0}{\tau}\frac{(1+g\tau)z+(1-g\tau)}{(1+g\tau_0)z+(1-g\tau_0)}, \tag{24}$$

where

$$g = \frac{2\pi f_p}{\tan(\pi f_p / f_s)} \tag{25}$$

with f_p being the bandwidth of interest and f_s being the sampling rate. It turns out that $F(z)$ is always stable since its pole is inside the unit circle.

In summary, the normal velocity can be calculated for a point source using the following formula:

$$u_n(z) = \frac{1}{\rho c}(\mathbf{n} \cdot \mathbf{e}_r)F(z)p(z). \tag{26}$$

The instantaneous normal intensity is simply

$$I_n(\mathbf{x}, n) = p(\mathbf{x}, n)u_n(\mathbf{x}, n). \tag{27}$$

Similar procedure applies to a collection of point sources, where the sound field can be calculated using the principle of superposition.

2.2. Fast multichannel inverse filtering

The aforementioned multichannel inverse filtering is carried out entirely in the time domain and is thus computationally intensive. To ease this problem, a technique based on the Eigensystem Realization Algorithm (ERA) [30] is exploited to simplify the NESI processing. This method establishes the following minimal state-space realization for linear systems:

$$\mathbf{x}(n+1) = \mathbf{A}_e\mathbf{x}(n) + \mathbf{B}_e\mathbf{u}(n), \tag{28}$$

$$\mathbf{y}(n) = \mathbf{C}_e\mathbf{x}(n) + \mathbf{D}_e\mathbf{u}(n), \tag{29}$$

where n is the discrete-time index, $\mathbf{x}(n)$ is the state vector, $\mathbf{u}(n)$ is the $M \times 1$ input vector, $\mathbf{y}(n)$ is the $J \times 1$ output vector, and $\mathbf{A}_e$, $\mathbf{B}_e$, $\mathbf{C}_e$ and $\mathbf{D}_e$ are constant matrices. The ERA starts with the impulse response matrices of the inverse filters:

$$\mathbf{C}(n) = \begin{bmatrix} c_{11}(n) & c_{12}(n) & \cdots & c_{1M}(n) \\ c_{21}(n) & c_{22}(n) & \cdots & c_{2M}(n) \\ \vdots & \vdots & \ddots & \vdots \\ c_{J1}(n) & c_{J2}(n) & \cdots & c_{JM}(n) \end{bmatrix}, \quad n = 0, 1, \ldots, N, \tag{30}$$

where n is the time index and N is the length of impulse response. Assemble these impulse response matrices into a J's $\times$ M's Hankel matrix:

$$\mathbf{H}(n-1) = \begin{bmatrix} \mathbf{C}(n) & \mathbf{C}(n+1) & \cdots & \mathbf{C}(n+s-1) \\ \mathbf{C}(n+1) & \mathbf{C}(n+2) & \cdots & \mathbf{C}(n+s) \\ \vdots & \vdots & \ddots & \vdots \\ \mathbf{C}(n+s-1) & \mathbf{C}(n+s) & \cdots & \mathbf{C}(n+2s-1) \end{bmatrix}, \tag{31}$$

where the s is an integer that determines the size of the matrix. Usually, s is taken to be $N/2$. Factor the Hankel matrix $\mathbf{H}(0)$ using singular value decomposition (SVD) as

$$\mathbf{H}(0) = \mathbf{U}\Sigma\mathbf{V}^H, \tag{32}$$

where $\mathbf{U}$ and $\mathbf{V}$ are unitary matrices and Σ is a diagonal matrix with singular values in its main diagonal. Great reduction is possible by observing the singular value plot. A typical example of singular value plot is shown in Fig. 3. The singular valves after $v = 100$ is very small and can be replaced by zeros. Hence, the matrices $\mathbf{U}$, $\mathbf{V}$, and Σ are in effect truncated. Based on the above SVD result, the minimal realization of $\mathbf{A}_e$, $\mathbf{B}_e$, $\mathbf{C}_e$, and $\mathbf{D}_e$

then follows:

$$\mathbf{A}_e = \Sigma^{-1/2}\mathbf{U}^H\mathbf{H}(1)\mathbf{V}\Sigma^{-1/2}, \quad \mathbf{B}_e = \Sigma^{1/2}\mathbf{V}^H\mathbf{E}_M,$$
$$\mathbf{C}_e = \mathbf{E}_J^H\mathbf{U}\Sigma^{1/2} \quad \text{and} \quad \mathbf{D}_e = \mathbf{C}(0), \tag{33}$$

where $\mathbf{E}_M^H = [\mathbf{I}_M \quad \mathbf{0}_M \quad \cdots \quad \mathbf{0}_M]$ and $\mathbf{E}_J^H = [\mathbf{I}_J \quad \mathbf{0}_J \quad \cdots \quad \mathbf{0}_J]$, and the $\mathbf{I}$ is an identity matrix and the $\mathbf{0}$ is a null matrix.

Instead of direct convolution in the time-domain, the multichannel filtering is efficiently carried out using the minimally realized state-space equation. This can give rise to considerable computational saving for the NESI processing owing to the fact that $v \ll Ms$ in general. For example, if $M = J = 30$ and $N = 227$, $M \times J \times 227 = 204{,}300$ multiplications are required using direct convolution, whereas only $v^2 + vM + Jv + JM = 22{,}500$ multiplications are required using the ERA with $v = 120$. Almost one order of reduction has been attained.

2.3. Criteria for array configuration

In configuring the array, there are many design factors to be taken into account. An in-depth investigation conducted in Ref. [27] has arrived at the following conclusions. The reconstruction performance achievable by the array is dependent on the condition number of the propagation matrix. The inverse problem is well conditioned when the number of sources and sensors is small, when the geometrical arrangement of sensors is conformal to the source geometry in terms of location, orientation and spacing, when the sensor array is positioned symmetrically with respect to the source array, and when the distance of reconstruction (DOR) is small.

The last point regarding the DOR is crucial to the performance of the NESI. It is well known in acoustics that the evanescent waves carrying the details in the nearfield will rapidly decay with distance to the farfield. The propagation matrix then becomes ill-conditioned as one attempts to reconstruct the sound image based on an already smoothed farfield measurement. In Fig. 4, a numerical simulation conducted for a 1D array shows in more detail what the effects of some array parameters have on the matrix conditioning. From Fig. 4(a), the condition number drops with increasing kd. The condition number of reconstruction with large L is higher than that of reconstruction with small L. Because condition number is defined as the ratio of the maximum singular value and the minimum singular value, the singular value plot in Fig. 4(b) further exhibits the same trend of matrix conditioning versus the DOR. In this work, the condition number during sound field reconstruction is generally kept under 10^3.

The procedures in choosing array parameters in this paper can be summarized as follows:

1. Choose the microphone spacing according to the maximum frequency ($f_{\max}$). A conservative rule is $d = \lambda/2$.
2. Choose the array aperture (D) that covers the source surface size.
3. The last two steps determine the number of microphone needed, $N_m = D/d$ for a 1D uniform linear array (ULA).

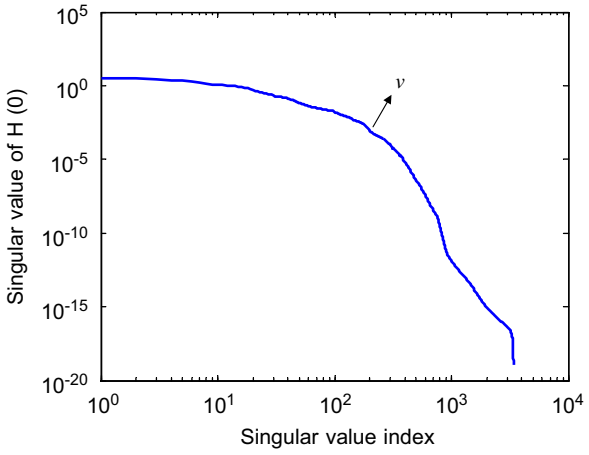

Fig. 3. Singular values of the Hankel matrix $\mathbf{H}(0)$. The singular values above the order vare negligibly small.

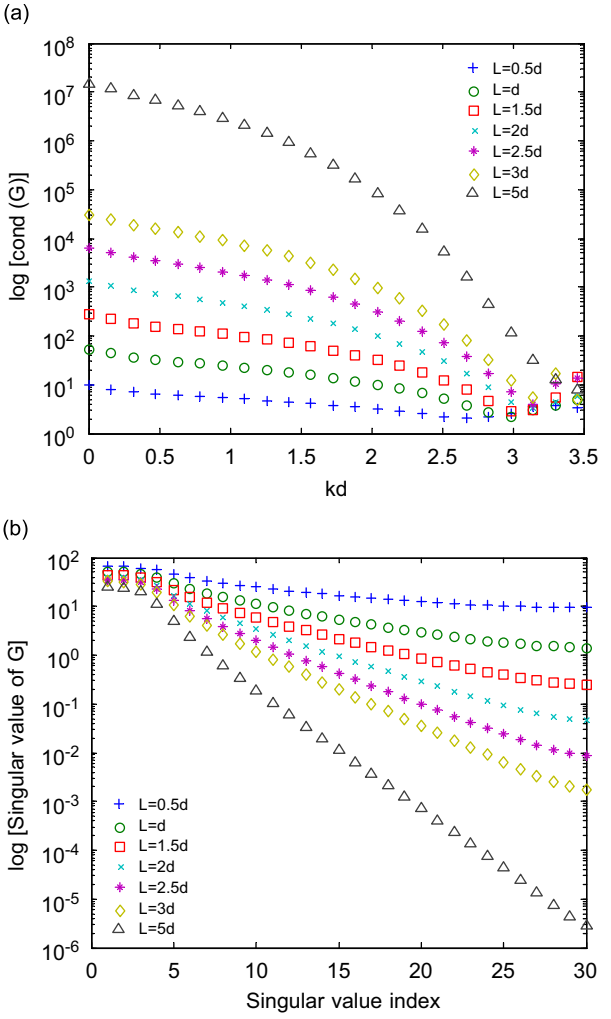

Fig. 4. Variation of condition number of propagation matrix for a 1D array. (a) Condition number vs. kd, (b) singular value distribution of propagation matrix (frequency = 200 Hz, the spacing between microphones and between focal points $d = d_f = 0.0858$ m and $kd = 0.3142$). The parameter k is the wave number, d is the spacing of array, G is the propagation matrix, and L is the DOR. There are 30 microphones and 30 focal points. The number of null points is one at each end.

4. Choose the DOR according to the condition number of propagation matrix and the array parameters determined above. As a rule of thumb, keep the condition number under 10^3.

2.4. The NAH with Wiener inverse filter

In this section, the NAH is briefly reviewed. The NAH serves to reconstruct a 3D sound field from the 2D hologram data scanned above the source surface. The 2D spatial Fourier transformation is employed to transform the space domain to the wave number domain, and vice versa:

$$\tilde{p}(k_x, k_y, z) \triangleq \int_{-\infty}^{\infty}\int_{-\infty}^{\infty} p(x, y, z) e^{j(k_x x + k_y y)}\, dx\, dy, \tag{34}$$

$$p(x, y, z) \triangleq \frac{1}{4\pi^2}\int_{-\infty}^{\infty}\int_{-\infty}^{\infty} \tilde{p}(k_x, k_y, z) e^{-j(k_x x + k_y y)}\, dk_x\, dk_y, \tag{35}$$

where x, y, and z are the Cartesian coordinates, d_x and d_y are the spacing of microphones in the x and y directions, and k_x and k_y are the wave number components in the x and y directions. In the k-domain, the sound pressure data of the reconstruction plane and the hologram plane can be related by

$$\tilde{p}(k_x, k_y, z) = \tilde{p}(k_x, k_y, z_H)\mathrm{e}^{-\mathrm{j}k_z(z-z_H)}, \tag{36}$$

where k_z is the wave number in the z direction. In Eq. (36), let $H(k_x, k_y) = \mathrm{e}^{-\mathrm{j}k_z(z-z_H)}$. In the paper, the Wiener inverse filter is employed to mitigate the ill-posedness during inverse reconstruction using NAH:

$$W(k_x, k_y) = \frac{1}{H(k_x, k_y)} \frac{1}{1 + (\alpha/|H(k_x, k_y)|^2)}, \tag{37}$$

where α is a regularization parameter. With the Wiener inverse filter, Eq. (36) can be rewritten as

$$\tilde{p}(k_x, k_y, z) = \tilde{p}(k_x, k_y, z_H)W(k_x, k_y). \tag{38}$$

Sound pressure can be reconstructed by the inverse Fourier transform in Eq. (35). The particle velocity can be calculated by using

$$\tilde{\mathbf{u}}(k_x, k_y, z) = \frac{\mathbf{k}}{\rho\omega}\tilde{p}(k_x, k_y, z), \tag{39}$$

where $\omega = 2\pi f$ and $\mathbf{k} = (k_x, k_y, k_z)$. The active intensity can be calculated with

$$\mathbf{I} = \tfrac{1}{2}\mathrm{Re}\{\tilde{p}\tilde{\mathbf{u}}\}. \tag{40}$$

3. Numerical simulations

In order to validate the proposed NESI technique, numerical simulations are conducted for a ULA and a 2D uniform rectangular array (URA). The inverse time-domain filers were designed off-line in light of the aforementioned procedures. The DOR (L) is selected such that the condition number of propagation matrix is less than 10^3. The sound pressure data are assumed to be received simultaneously at all microphones and the processing is carried out in real time fashion. During processing, the state-space form obtained using the ERA was employed to enhance computation efficiency. In addition, the numerical simulation using the NAH approach is conducted to compare with the NESI. The assumptions about the sources used in the simulation are summarized as follows:

(a) Only outgoing waves are present.
(b) The array aperture covers the main area of the noise sources.
(c) The time-domain waveform of noise sources are Gaussian random noise.
(d) All sources are driven by the 'same' signal.

3.1. One-dimensional array (ULA)

A simulation is undertaken for the ULA with structure shown in Fig. 2(a). In the "square" case in which the number of microphones (M) is equal to the number of the focal points (J). Specifically, $M = J = 30$ in this simulation. The spacing of microphones (d) and the spacing of focal points (d_f) are both 0.0858 m. DOR (L) is chosen to be 0.1286 m and retreated distance (L_r) is chosen to be $d/20$. For this DOR, the condition number is well below 10^3, as shown in Fig. 5(a). In the inverse filter design, the regularization parameter β was selected to be 1/1000 of the maximum singular value of **G**. Fig. 5(b) shows the frequency response magnitude of four selected filters. The responses obtained using the ERA-based state-space form are in close agreement with the original. With the state-space form, the computation efficiency is improved by the ratio of direct convolution to ERA is 13:1. Four random noise sources driven by the same signal band-limited to 2.5 kHz are situated at 0.0858, 1.2005, 1.2863, and 2.4010 m, respectively, from the left end on the focal surface. Of these four sources, two sources are very close to each other (within one spacing) at the center, whereas the other two sources are very close to the ends. A question naturally arises here. With such small DOR, will the pressure measurement

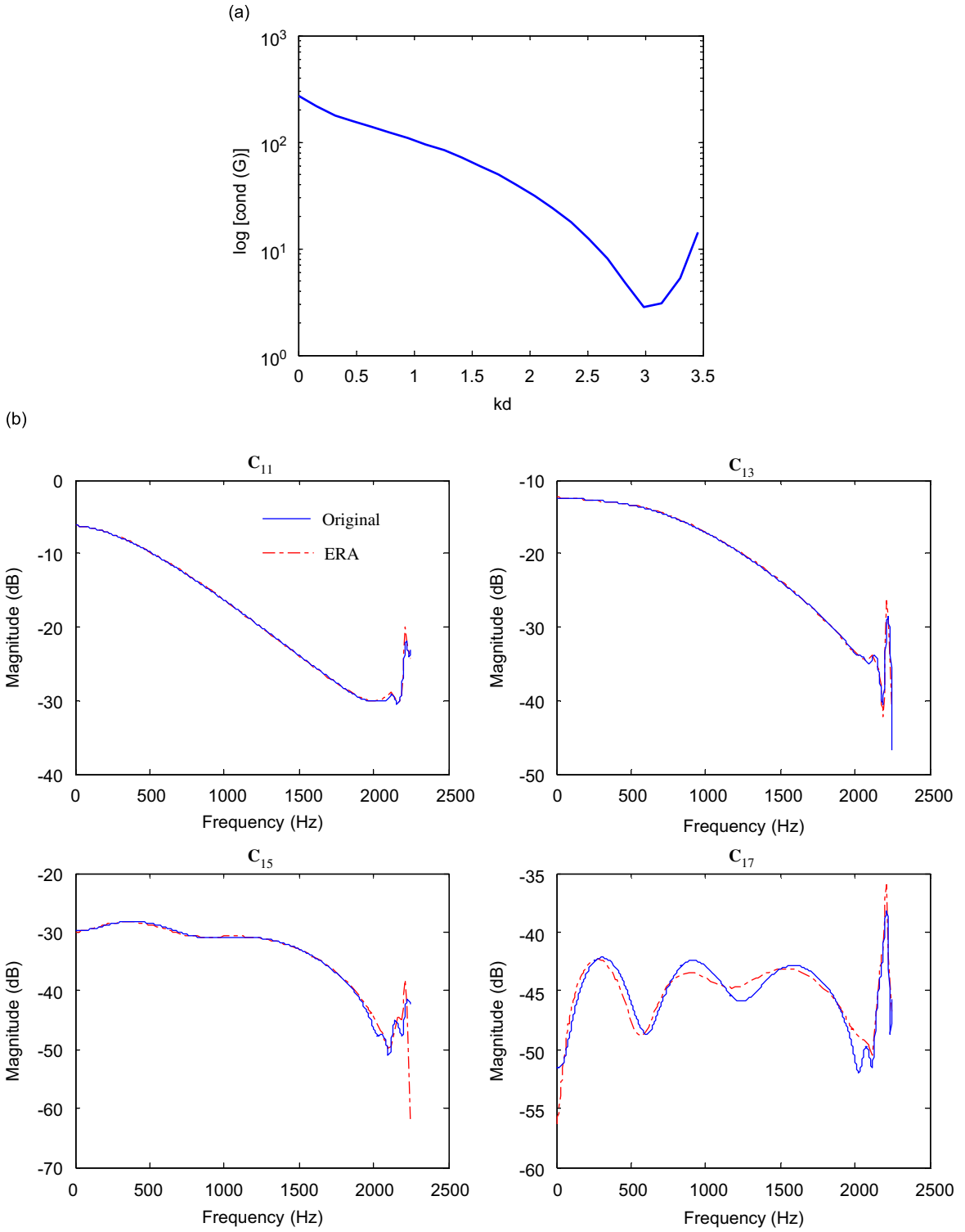

Fig. 5. The simulation of ULA (square case). (a) Condition number of propagation matrix, (b) frequency responses of $\mathbf{C}_{11}$, $\mathbf{C}_{13}$, $\mathbf{C}_{15}$, and $\mathbf{C}_{17}$ calculated by the ERA, (c) rms sound pressure image on the microphone surface, (d) rms source strength image on the focal surface, (e) rms sound pressure image on the reconstruction surface, (f) rms particle velocity image on the reconstruction surface, (g) rms sound intensity image on the reconstruction surface, and (h) rms source strengths between the calculated results and the set values. Arrows are used to indicate the source positions.

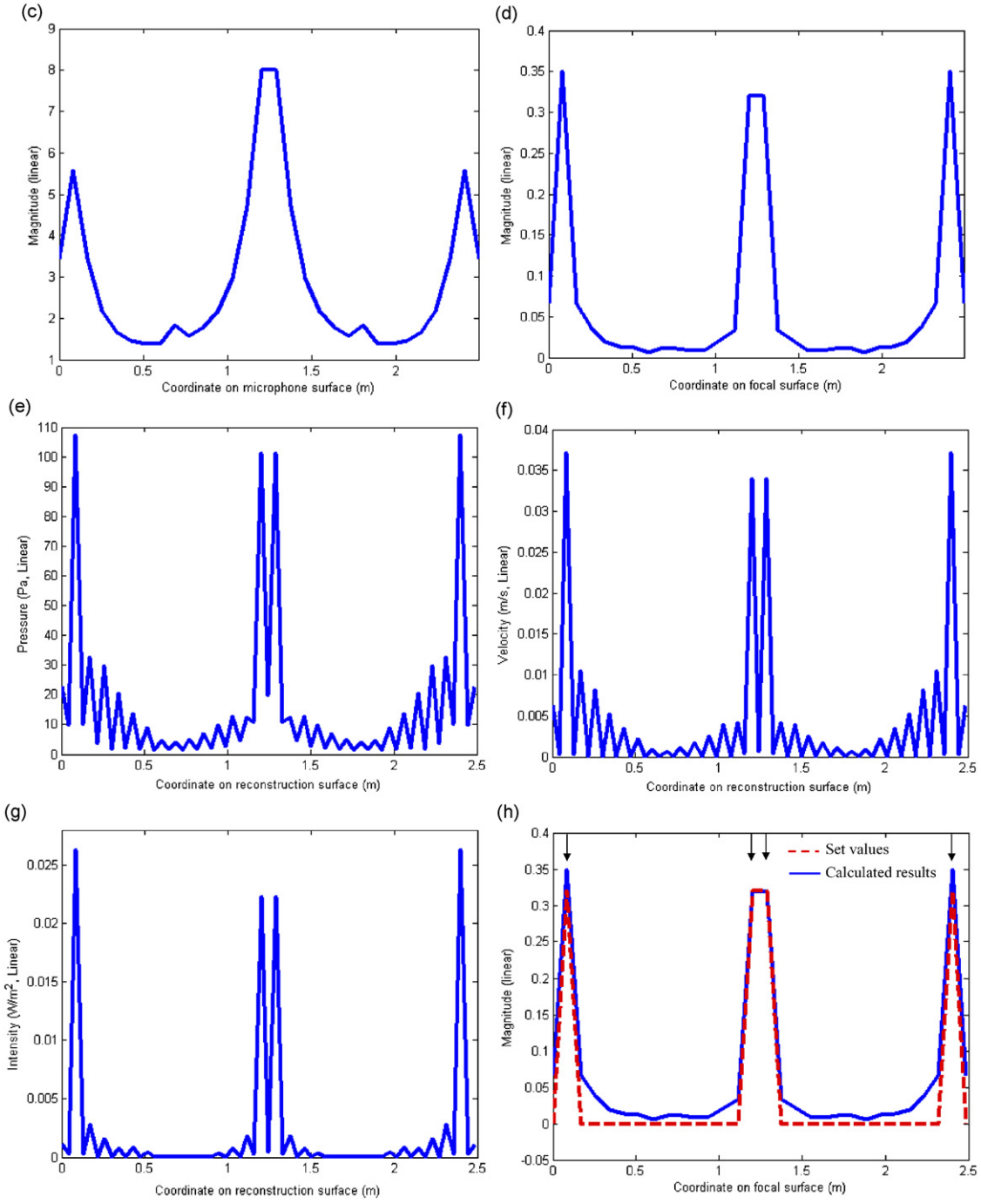

Fig. 5. (*Continued*)

of the microphone reveal the source locations already? Fig. 5(c) shows the unprocessed root-mean-squares (rms) sound pressure received at the microphones that is defined as

$$\mathrm{rms}(\mathbf{p}) = \sqrt{\frac{\sum_{n=1}^{N}[P_m(n)]^2}{N}}, \quad m = 1, 2, \ldots, M, \tag{41}$$

where n denotes the discrete-time index. The adjacent two sources at the center are barely resolvable in the rms plot. This counter-intuitive result indicates unprocessed pressure measurement is insufficient to identify noise sources. The NESI with focal points retreated by $d/20$ is then applied to process the same data and the source strength is shown in Fig. 5(d). Since there are only 30 focal points on the plot, the adjacent two sources (within one spacing) are still not resolvable. However, if the sound pressure, particle velocity, and intensity are

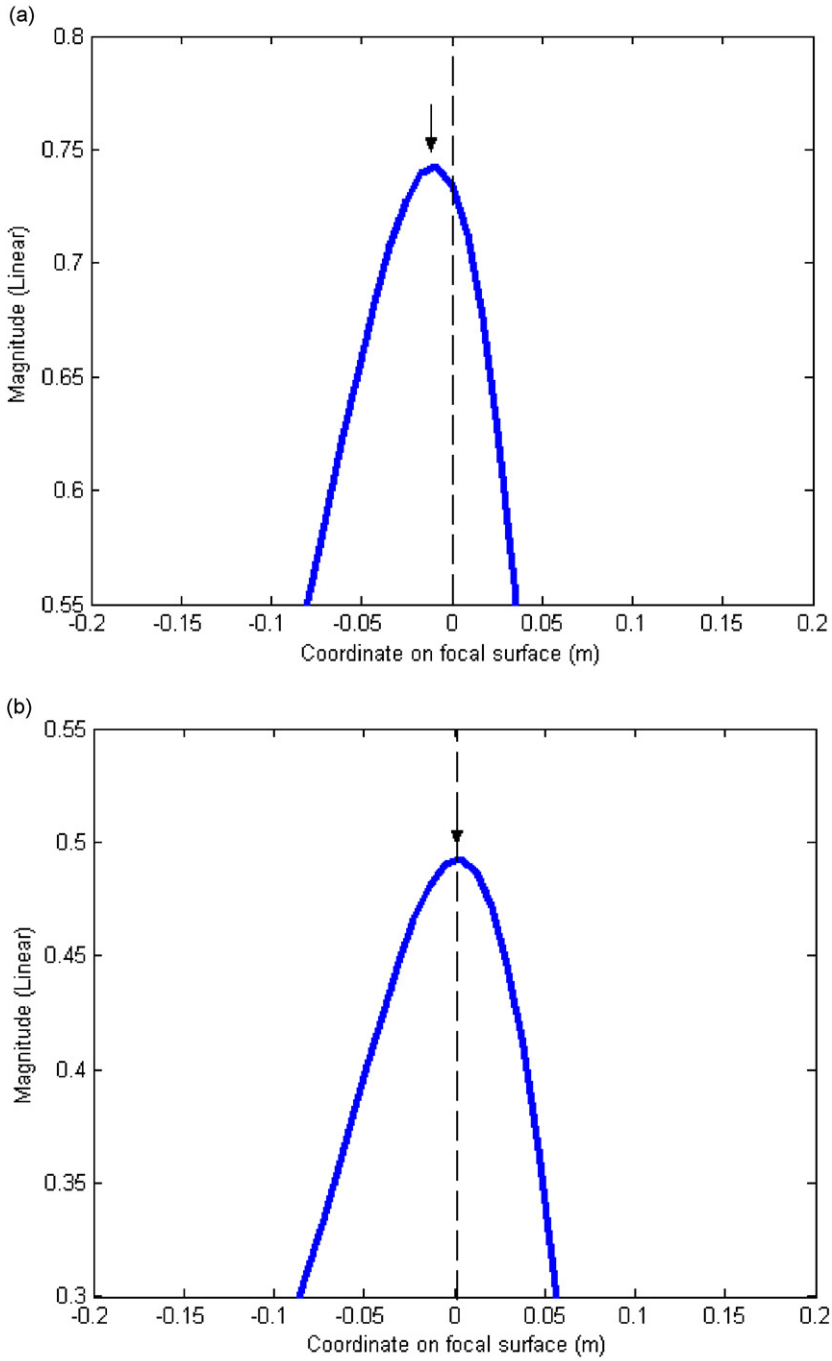

Fig. 6. The beam pattern at the boundary of the focal surface: (a) without window design and (b) with window design.

calculated based on the above source strength, all four sources are clearly resolvable in Fig. 5(e)–(g). The spatial resolution of the NESI with retreated focal point technique is apparently superior to that of straight rms measurement. Fig. 5(h) shows the source strengths between the calculated results and the set values. From the result, nearly perfect match can be observed in these source strengths between the calculated results and the set values.

Next, the NESI is tested for an under-determined case in which $M = 30$ and $J = 45$. The other parameters are $d = 0.0858$ m, $d_f = 0.056517$ m, $L = 0.1286$ m, and $L_r = d/20$. To mitigate boundary defocusing problem, one null point is allocated outside boundary on each side. Fig. 6 shows the beam pattern at the left boundary. This figure shows that the main-lobe is focused at 0 m with the window design, but is not focused without the window design. In the inverse filter design, the regularization parameter β was selected to be 2/3 of the maximum singular value of $\mathbf{G}$. In addition, window design is used here because the boundary defocusing problem gets more severe in the under-determined case. The random sources with equal strength and band-limited to 2.5 kHz are assumed to be on the focal surface at 0.0565, 1.2434, 1.2999, and 2.4302 m, respectively, from the left. Fig. 7(a) shows the unprocessed rms sound pressure received at the microphones. The source strengths calculated using the NESI with and without window design are shown in Figs. 7(b) and (c). The NESI with window design are clearly identifiable at both ends. Although noise sources are resolvable by the NESI without window design, improved quality of image is attained using the window design. Figs. 7(c) and

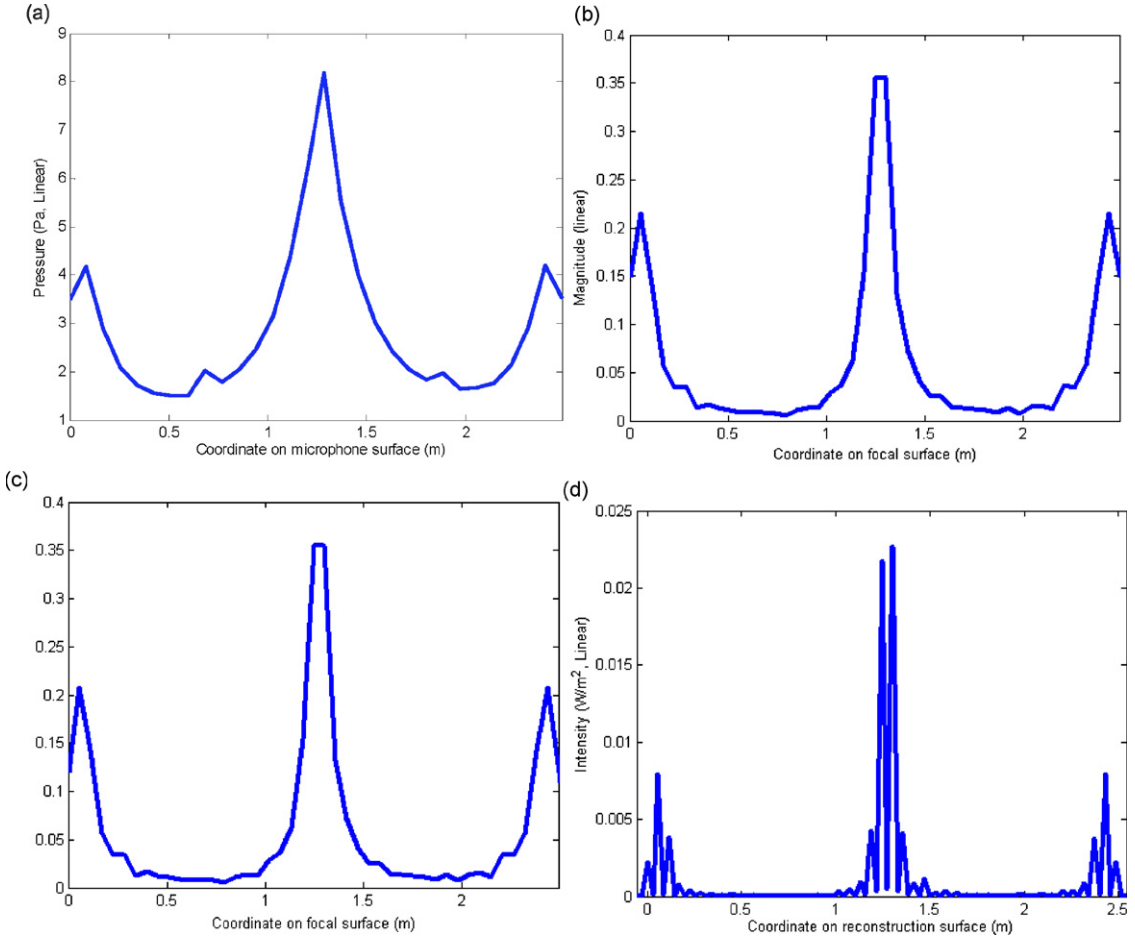

Fig. 7. The simulation of ULA (under-determined case): (a) Rms sound pressure image on the microphone surface, (b) rms source strength image without window design on the focal surface, (c) rms source strength image with window design on the focal surface, and (d) rms sound intensity image on the reconstruction surface.

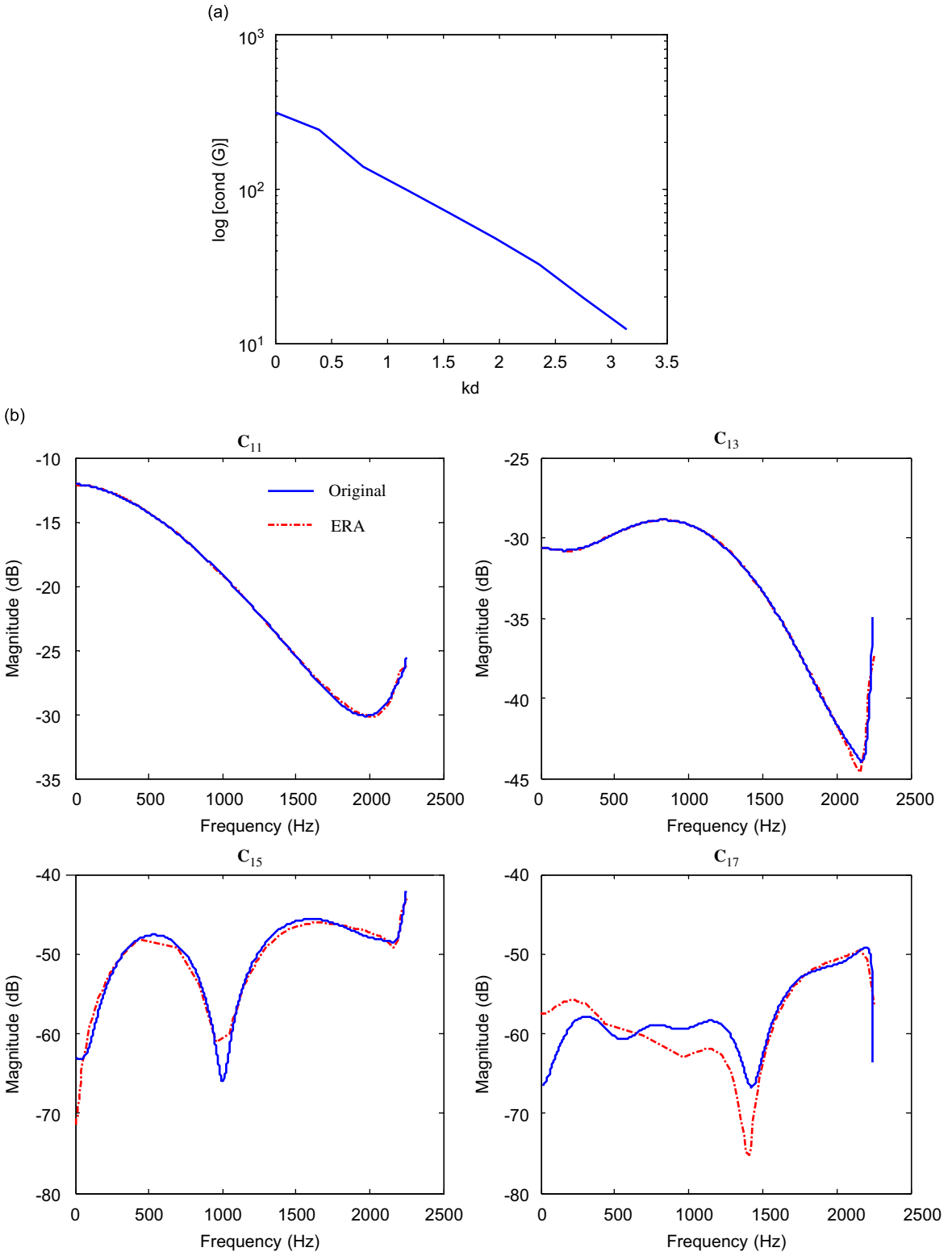

Fig. 8. The simulation of URA (square case): (a) condition number of propagation matrix, (b) frequency responses of $\mathbf{C}_{11}$, $\mathbf{C}_{13}$, $\mathbf{C}_{15}$, and $\mathbf{C}_{17}$ calculated by the ERA, (c) distribution of noise sources, (d) rms sound pressure image on the microphone surface, (e) rms source strength image on the focal surface, (f) rms sound pressure image on the reconstruction surface, (g) rms particle velocity image on the reconstruction surface, (h) rms sound intensity image on the reconstruction surface, and (i) rms source strengths between the calculated results and the set values for the sources along the line (x, 0.3434 m). Arrows are used to indicate the source positions.

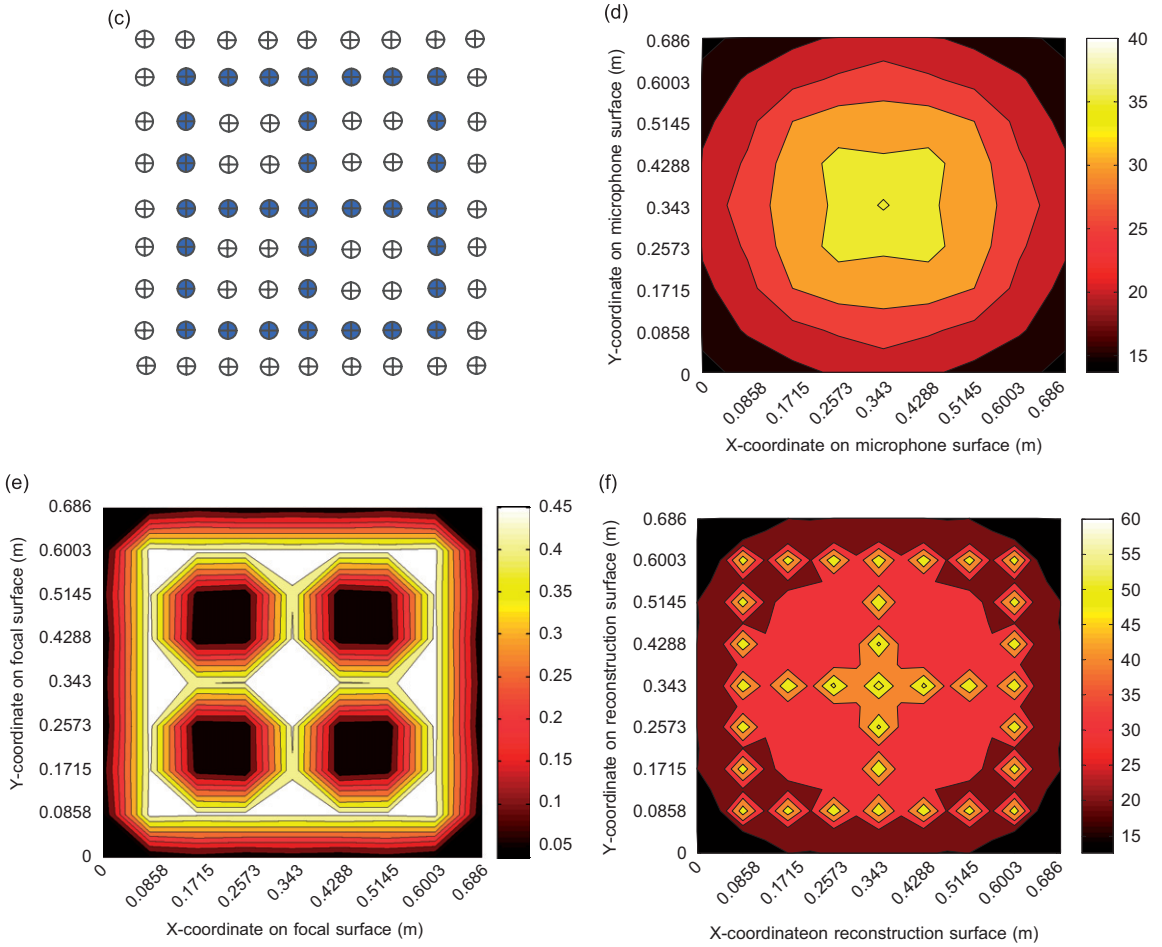

Fig. 8. (*Continued*)

(d) illustrate the source strength, and the sound intensity obtained using the NESI with retreated focal point technique. In contrast to the barely unresolvable result of the rms plot (Fig. 7(a)), two separate peaks are clearly visible at the center region in the NESI results (Fig. 7(c)).

3.2. Two-dimensional array (URA)

In this section, the NESI is examined for a 2D URA. The array parameters are $M = J = 9 \times 9$ (the square case), the spacing between microphones and between focal points $d = d_f = 0.0858$ m, the DOR, $L = d$ and retreated distance $L_r = d/20$. The condition number of the propagation matrix is plotted versus kd in Fig. 8(a). The NESI inverse filters are then designed using a regularization parameter β being 1/1000 of the maximum singular value of $\mathbf{G}$. The frequency responses of some selected inverse filers without and with ERA are compared in Fig. 8(b). The inverse filters are implemented using the ERA-based state-space form to enhance computation efficiency. The ratio of the number of multiplications of the direct convolution to the ERA is approximately 15:1. Assume that random noise sources band-limited to 2.5 kHz are distributed like a Chinese character "⊞", as shown in Fig. 8(c). All random noise sources are driven by the 'same' signal. Fig. 8(d) shows the unprocessed rms sound pressure received at the microphones. Figs. 8(e)–(h) illustrate the source strength, the sound pressure, the particle velocity, and the sound intensity obtained using the NESI with retreated focal point technique. In contrast to the totally unresolvable result of the rms plot (Fig. 8(d)), the Chinese character are clearly identifiable in the NESI results (Figs. 8(f)–(h)), particularly in the velocity and

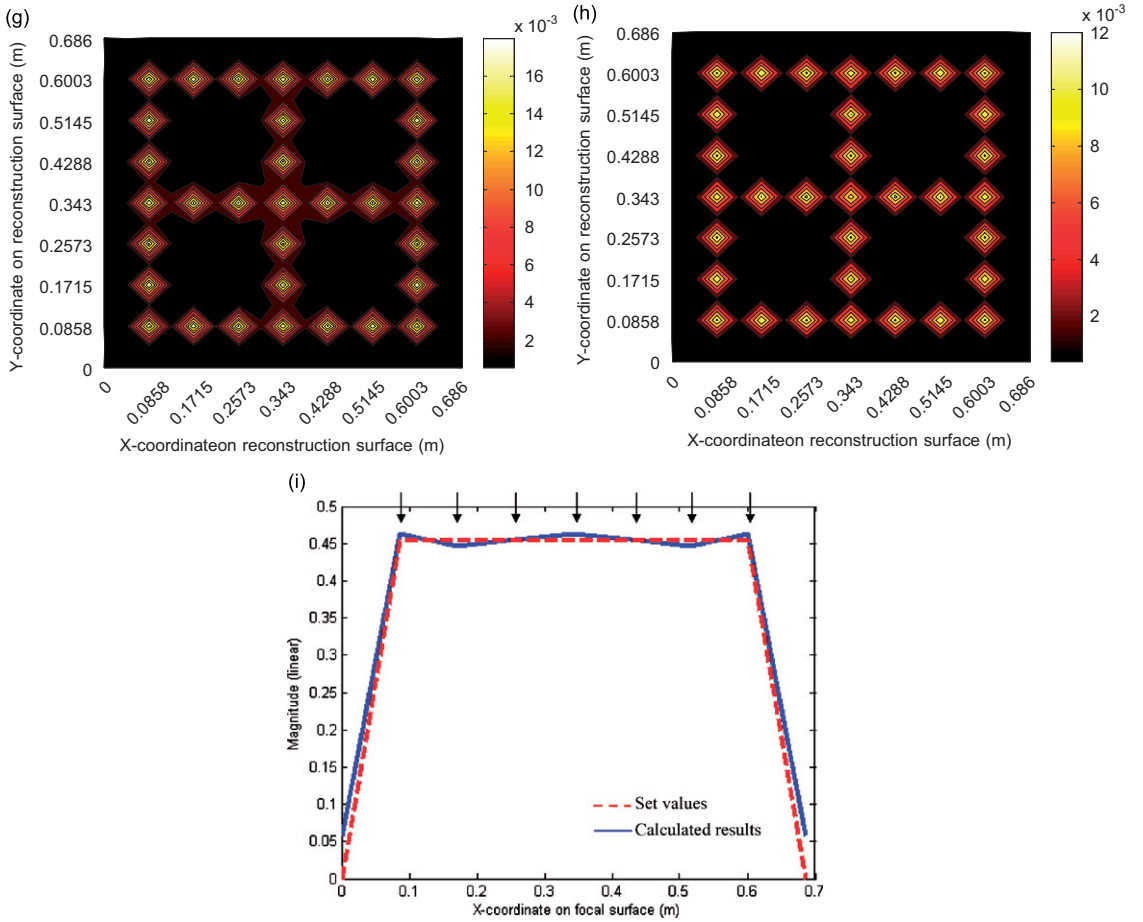

Fig. 8. (*Continued*)

intensity plots. The frequency responses obtained using the ERA-based state-space form are in close agreement with the original. Fig. 8(i) shows the source strengths between the calculated results and the set values. From the result, nearly perfect match can be observed in these source strengths between the calculated results and the set values.

The next simulation is conducted for the under-determined case in which the spatial resolution is improved over the preceding square case. In this simulation, $d = 0.0858$ m, $d_f = 0.0686$ m, $L = d$, $L_r = d/20$, $M = 9 \times 9$, the J is 11×11, β is selected to be 1/1000 of the maximum singular value of $\mathbf{G}$, and one layer of null points are padded outside the boundary. The beam pattern associated with the focal point (0, 0) is shown in Fig. 9. The maximum of the beam for the NESI without windowing is located at $(-0.01, -0.01)$, which is slightly off the target. By contrast, with window design, the maximum of the beam is located right at (0, 0). The beam appears to be better shaped in that its pattern has a sharper main-lobe and smaller side lobes. In this setting, the NESI with windowing is applied to reconstruct random sources which are distributed as the Chinese character "⊞" shown in Fig. 10(a). All random sources are driven by the same signal band-limited to 2.5 kHz. Fig. 10(b) shows the unprocessed rms sound pressure received at the microphones. Fig. 10(c) and (d) illustrate the identified source strength, and the sound intensity obtained using the NESI with retreated focal point technique. In contrast to the totally unresolvable result of the rms plot (Fig. 10(b)), the Chinese character are clearly identifiable in the NESI results (Fig. 10(c) and (d)), particularly in the intensity plots.

In the last simulation, the NESI is applied to a Gaussian-shaped transient noise. Fig. 11(a) shows the time-domain wave form of the transient noise. The array parameters are: $M = J = 9 \times 9$ (the square case), $d = d_f = 0.0858$ m, $L = d$, and $L_r = d/20$. In the inverse filter design, the frequency-dependent regularization

parameter β was selected to be 1/1000 of the maximum singular value of **G**. Assume that transient noise sources are distributed spatially like a Chinese character "⊞". The unprocessed rms sound pressure received at the microphones is shown in Fig. 11(b). Figs. 11(c) and (d) illustrate the identified source strength, and the sound intensity obtained using the NESI with retreated focal point technique. From the results of Figs. 11(c) and (d), the Chinese character is clearly identifiable after the NESI, particularly in the intensity plots. This suggests that the NESI technique applies to not only stationary noises but also transient noises.

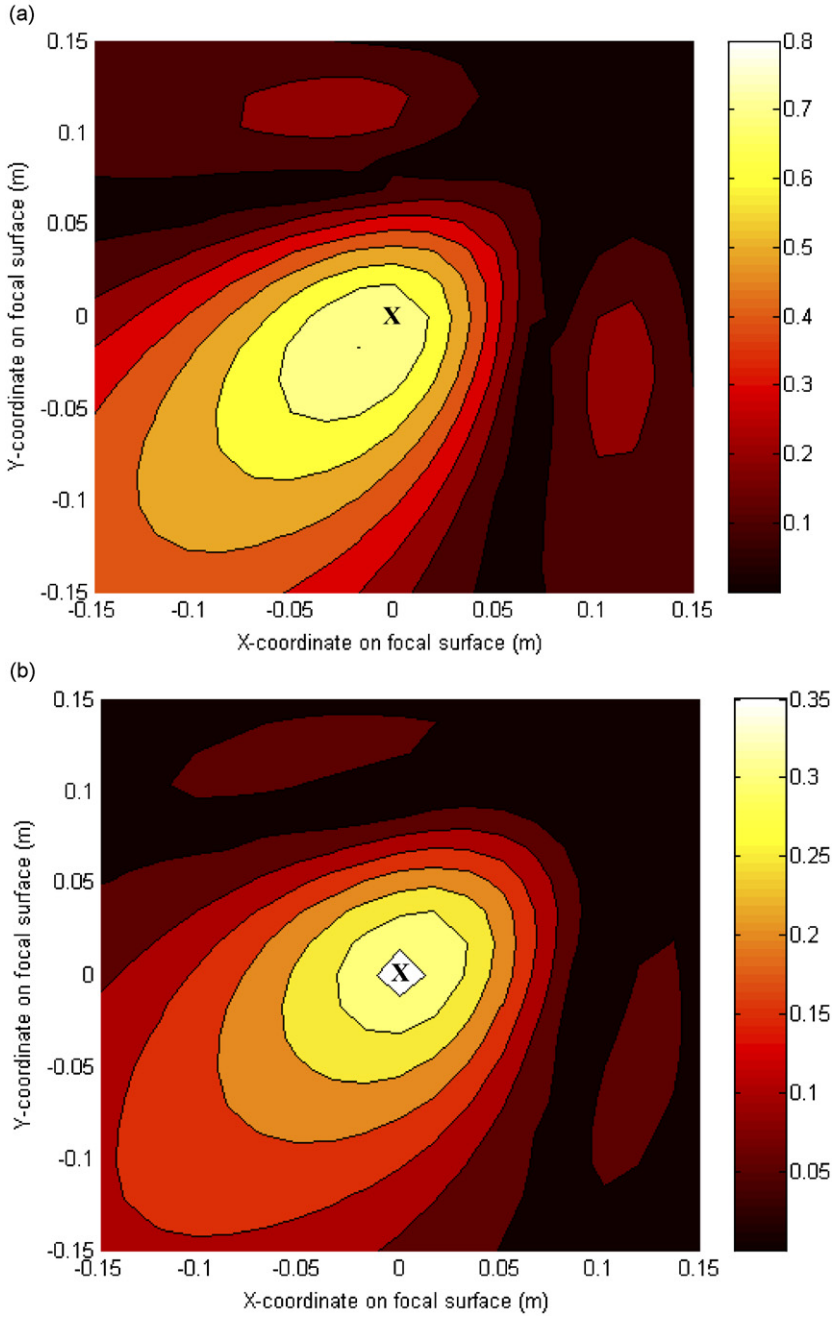

Fig. 9. The beam pattern at the boundary of the focal surface. The intended focal point (0, 0) is marked with "X" on the contour plot: (a) without window design and (b) with window design.

One final worth noting feature of the NESI is examined is the following simulation. In the NAH, the microphone spacing and the DOR are generally confined to be less than half of the wavelength, i.e., $d \leqslant \lambda/2$, at the $f_{\max}$. However, the over-conservative rule can be considerably relaxed in the NESI. Consider the NESI with the array parameters, $M = J = 9 \times 9$, $f_{\max} = 2\,\text{kHz}$, $d = d_f = \text{DOR}\ (L) = 0.5145\,\text{m} = 3\lambda$, $L_r = d/20$ and β is selected to be $1/1000$ of the maximum singular value of $\mathbf{G}$. The unprocessed rms sound pressure received at the microphones is shown in Fig. 12(a). The source strength and the sound intensity obtained using the NESI with retreated focal point technique are shown in Figs. 12(b) and (c) for contrast. With this substantially lager spacing and reconstruction distance (3λ), the NESI remains capable of resolving the broadband random noise sources.

3.3. The NAH with Wiener inverse filter

In this numerical simulation, the NAH is compared with the NESI. The array aperture is chosen to be identical to numerical simulation of the NESI. The NAH is essentially based on 2D FFT processing. If only a limited numbers of sensors are used for NAH, one possible consequence is that the aperture of array will be decreased if the microphone spacing is kept below half the wave length to avoid the k-domain aliasing. This would in turn result in poor k-domain resolution and undesired spatial domain aliasing. Conversely, should we choose to increase the microphone spacing to maintain a large enough aperture, we would run into another problem of k-domain aliasing (grating lobes). Therefore, to avoid the dilemma, we are eventually forced to

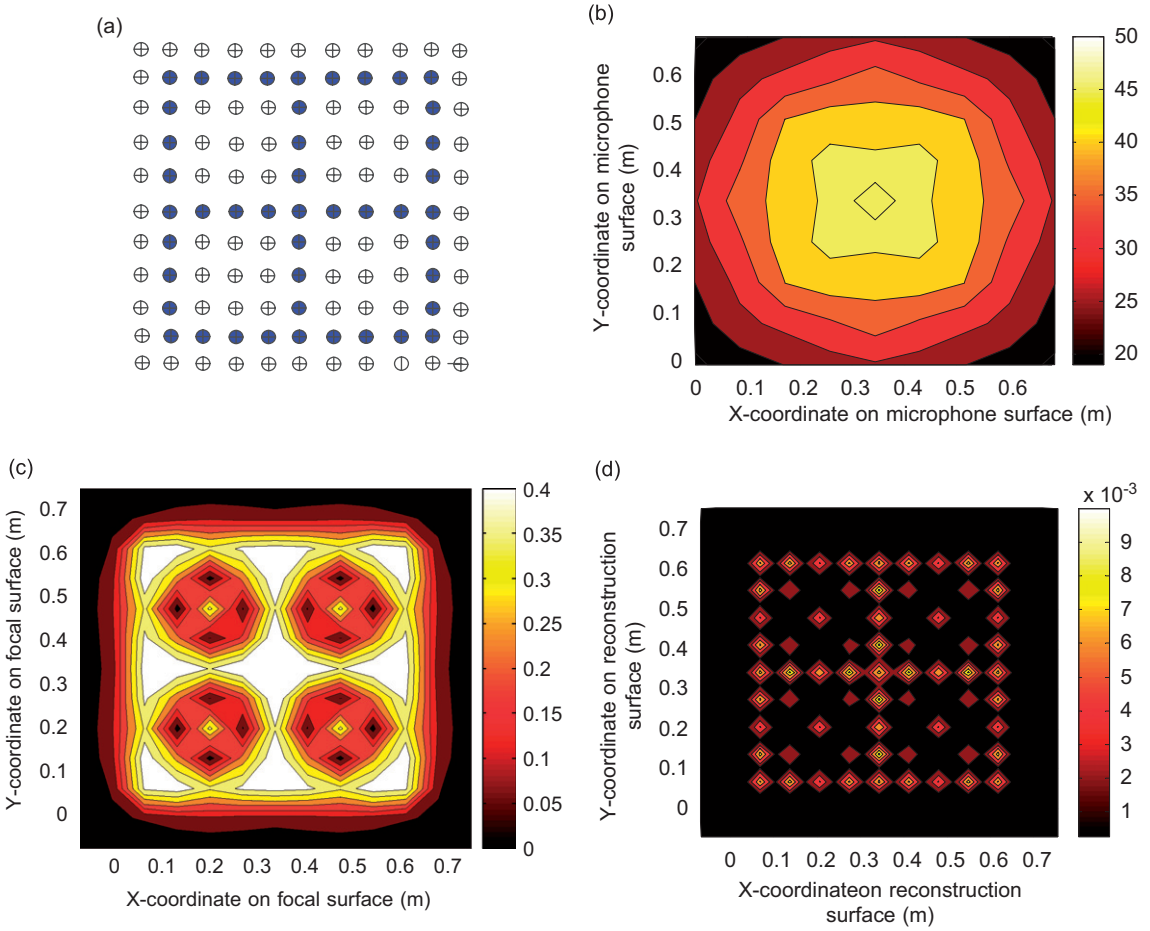

Fig. 10. The simulation of URA (under-determined case): (a) distribution of noise sources, (b) rms sound pressure image on the microphone surface, (c) rms source strength image on the focal surface, and (d) rms sound intensity image on the reconstruction surface.

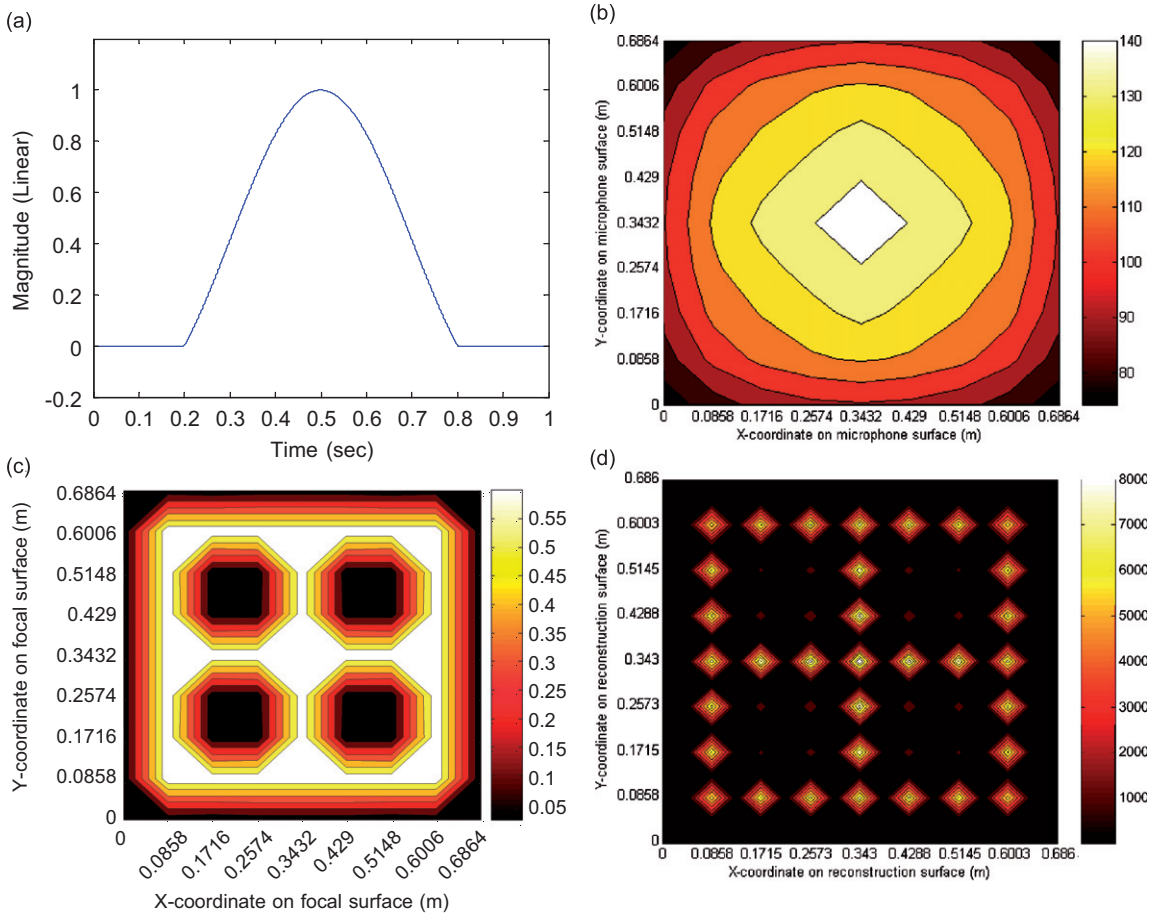

Fig. 11. The simulation of URA (square case): (a) the time-domain of the transient noise in one-second duration, (b) rms sound pressure image on the microphone surface, (c) rms source strength image on the focal surface, and (d) rms sound intensity image on the reconstruction surface.

increase the channels of sensors to a very large number. On the other hand, NESI requires far lower channel count for imaging because it does not rely on indirect k-domain processing and thus the above-mentioned problems inherent to FFT can be waived. In the simulation, in order to identify the noise sources distributed as a Chinese character "⊞", it was found that a far higher number of channels (64×64) of microphones were necessary to attain satisfactory resolution. By contrast, only 9×9 microphones are sufficient using the NESI approach. In the simulation of NAH, the parameters of array are: $M = J = 64 \times 64$, the spacing between microphones and between focal points $d = d_f = 0.0109\,\text{m}$ ($\lambda/2$), $L = d$, $L_r = d/20$, and $\alpha = 0.08$. The NAH is designed for 1 kHz sinusoidal sources. Assume that the noise sources are distributed spatially like a Chinese character "⊞". All sources are driven by the same signal. The number and position of sinusoid noise sources are taken from numerical simulation of URA (square case). In addition, the noise sources are distributed the same as those in Fig. 8(c). Fig. 13(a) illustrate the unprocessed rms sound pressure received at the microphones. Figs. 13(b)–(d) show the pressure, velocity, intensity images reconstructed by the NAH with Wiener inverse filter. From the results, the Chinese character can be identified in the images reconstructed by the NAH. However, spillover problem is more pronounced near the boundary than that in the results obtained using NESI.

4. Conclusions

A new sound Field reconstruction technique, the NESI, has been proposed in this paper. This technique enables effective identification of noise sources based on sound pressure, particle velocity, and intensity

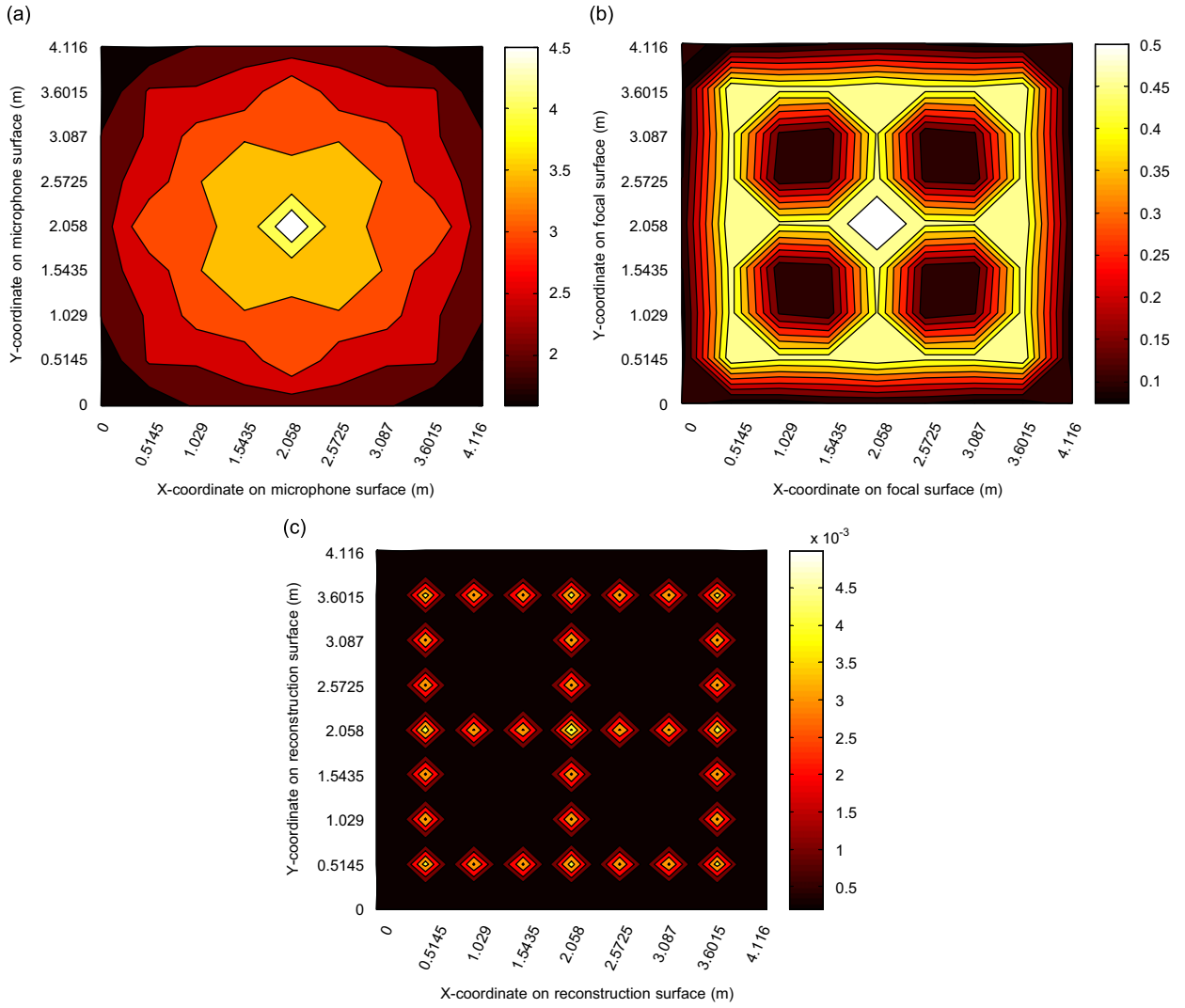

Fig. 12. The simulation of URA (square case). The microphone spacing and the DOR are both three times of the wavelength at the maximum frequency 2 kHz, i.e., $L = d = 3\lambda$. (a) rms sound pressure image on the microphone surface, (b) rms source strength image on the focal surface, and (c) rms sound intensity image on the reconstruction surface.

images. Inverse filters are design using the least-squares optimization with the aid of Tikhonov regularization. Criteria for choosing array parameters are summarized. In particular, the DOR is always selected to render the condition number of propagation matrix below 10^3. The window design is employed to alleviate boundary defocusing problem. Singularity problem is circumvented by using a retreated focal point technique. The state-space form obtained using the ERA is exploited to enhance computation efficiency for real-time implementation. The NESI technique has been validated through extensive numerical investigations for 1D and 2D arrays. The NESI proves effective in the identification of broadband random and transient noise sources. In addition, the NESI does not need as large channel count as the NAH approach.

The unique features of NESI are summarized as follows. Entire processing is carried out in the time-domain. By doing so, many of the limitations inherent in conventional FFT-based methods are eliminated. For example, the NESI applies to imaging of transient noise sources. The microphone number can be limited and the interelement spacing is not confined to the conservative $\lambda/2$ rule, but can be considerably larger. The method is also applicable to nonuniform and nonplanar arrays. Experimental investigation is currently on the way to further justify the practicality of NESI.

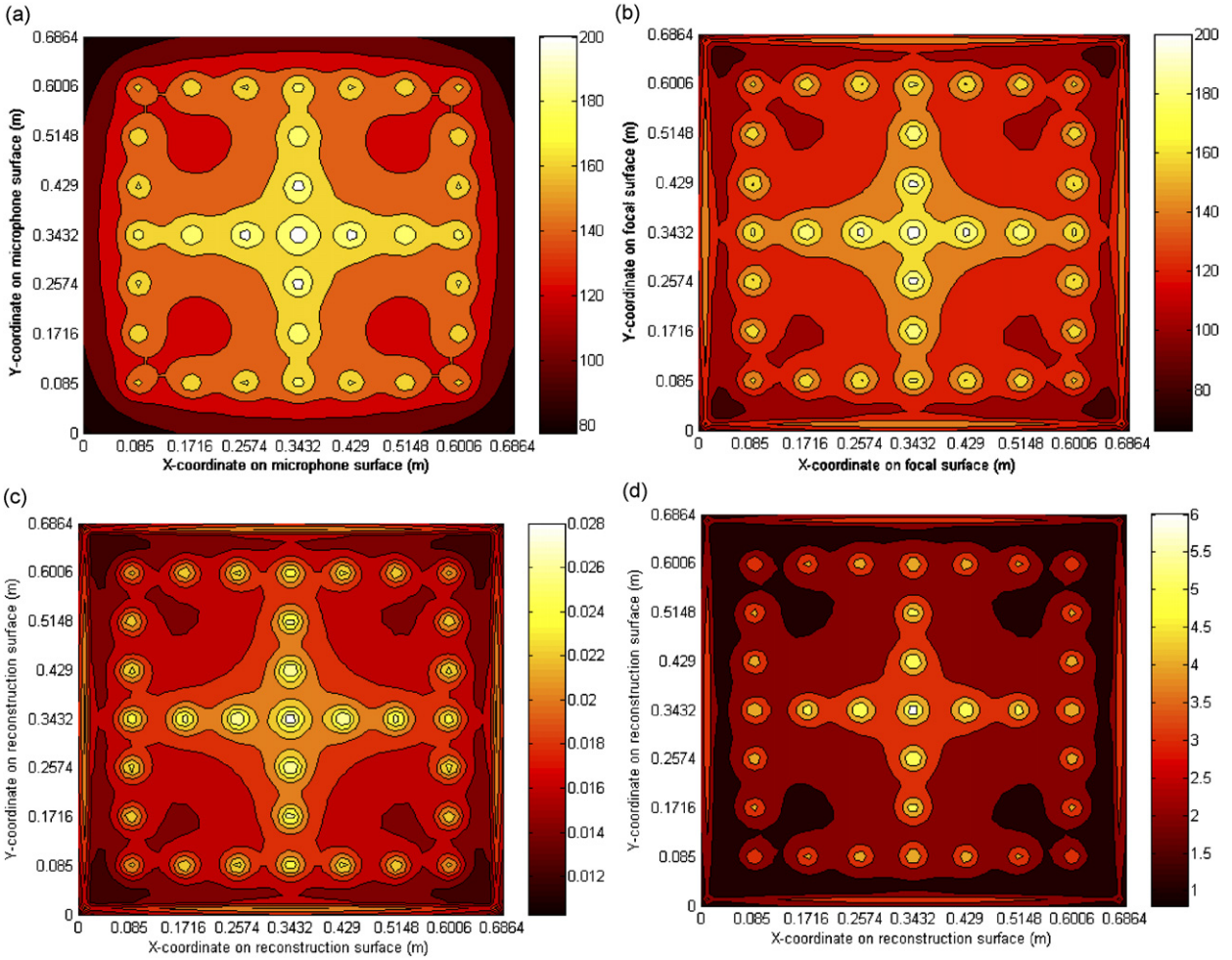

Fig. 13. The simulation of URA (square case) using the NAH approach, 1 kHz sinusoidal sources are used. (a) rms sound pressure image on the microphone surface, (b) sound pressure image on the reconstruction surface, (c) rms particle velocity image on the reconstruction surface, and (d) rms sound intensity image on the reconstruction surface.

Acknowledgments

The work was supported by the National Science Council in Taiwan, Republic of China, under the Project no. NSC94-2212-E-009-018.

References

[1] Y. Fan, B. Tysoe, J. Sim, K. Mirkhani, A.N. Sinclair, F. Honarvar, H. Sildva, A. Szecket, R. Hardwick, *Ultrasonics* 41 (2003) 369–375.
[2] M. Duquennoy, M. Ouaftouh, M. Ourak, *NDT & E International* 32 (1999) 189–199.
[3] V. Murino, *Pattern Recognition* 34 (2001) 981–997.
[4] D. Zha, T. Qiu, *Digital Signal Processing* 16 (2006) 149–163.
[5] U. Benko, J. Petrovcic, D. Juricic, J. Tavcar, J. Rejec, A. Stefanovska, *Journal of Sound and Vibration* 276 (2004) 781–806.
[6] J.D. Wu, C.Q. Chuang, *NDT&E International* 38 (2005) 605–614.
[7] E.G. Williams, J.D. Maynard, *Physics Review Letters* 45 (1980) 554–557.
[8] E.G. Williams, J.D. Maynard, E. Skuarzyk, *Journal of the Acoustical Society of America* 68 (1980) 340–344.
[9] J.H. Zhang, B. Han, *Mechanical Systems and Signal* 19 (2005) 213–221.

[10] J. Hald, STSF—a unique technique for scan-based nearfield acoustic holography without restriction of coherence, Brüel & Kjær Technical Review No. 1, 1989.
[11] J. Hald, STSF—practical instrumentation and application, Brüel & Kjær Technical Review No. 2, 1989.
[12] J. Hald, Non-stationary STSF, Brüel & Kjær Technical Review No. 1, 2000.
[13] E.G. Williams, *Fourier Acoustics*, Academic Press, New York, 1999.
[14] M.A. Rowell, D.J. Oldham, *Journal of Sound and Vibration* 180 (1995) 99–118.
[15] W.A. Veronesi, J.D. Maynard, *Journal of the Acoustical Society of America* 85 (1988) 588–598.
[16] M.R. Bai, *Journal of the Acoustical Society of America* 92 (1992) 533–549.
[17] G.V. Borgiotti, A. Sarkissian, E.G. Williams, L. Schuetz, *Journal of the Acoustical Society of America* 88 (1990) 199–209.
[18] M.R. Bai, J.W. Lee, *ASME, Journal of Vibration and Acoustics* 120 (1998) 426–433.
[19] J.J. Christensen, J. Hald, Beamforming, Brüel & Kjær Technical Review No. 1, 2004.
[20] J. Hald, Combined NAH and beamforming using the same array, Brüel & Kjær Technical Review No. 1, 2005.
[21] G.H. Koopmann, L. Song, J.B. Fahnline, *Journal of the Acoustical Society of America* 86 (1989) 2433–2438.
[22] L. Song, G.H. Koopmann, J.B. Fahnline, *Journal of the Acoustical Society of America* 89 (1991) 2625–2633.
[23] M.R. Bai, C.W. Tung, C.C. Lee, *Journal of the Acoustical Society of America* 117 (5) (2005) 2802–2813.
[24] B. Noble, *Applied Linear Algebra*, Prentice-Hall, Englewood Cliffs, NJ, 1988.
[25] Kirkeby, P.A. Nelson, H. Hamada, *IEEE Transactions on Speech and Audio Processing* 6 (1998) 189–194.
[26] A. Schuhmacher, J. Hald, *Journal of the Acoustical Society of America* 113 (2003) 114–127.
[27] P.A. Nelson, S.H. Yoon, *Journal of Sound and Vibration* 233 (2000) 643–668.
[28] P.M. Morse, K.U. Ingard, *Theoretical Acoustics*, Princeton University Press, Princeton, NJ, 1986.
[29] A.V. Oppenheim, R.W. Schafer, *Discrete-Time Signal Processing*, Prentice-Hall, Englewood Cliffs, NJ, 1989.
[30] J.N. Juang, *Applied System Identification*, Prentice-Hall PTR, Englewood Cliffs, NJ, 1994.